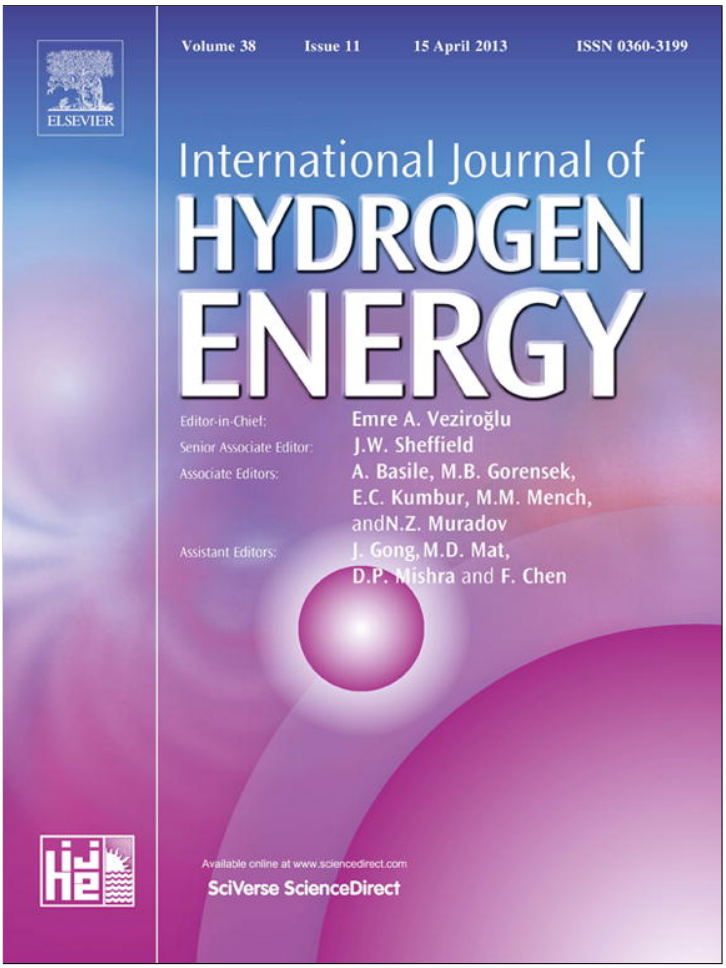

INTERNATIONAL JOURNAL OF HYDROGEN ENERGY 38 (2013) 4418–4428

Available online at www.sciencedirect.com

SciVerse ScienceDirect

journal homepage: www.elsevier.com/locate/he

Ethanol steam reforming for hydrogen generation over structured catalysts

Eduardo López [a,b,*], *Nuria J. Divins* [a,c], *Andrés Anzola* [b], *Susana Schbib* [b], *Daniel Borio* [b], *Jordi Llorca* [a,c]

[a] *Institut de Tècniques Energètiques, Universitat Politècnica de Catalunya, Diagonal 647, ed. ETSEIB, 08028 Barcelona, Spain*[1]
[b] *Planta Piloto de Ingeniería Química (CONICET-UNS), Camino de la Carrindanga km 7, 8000 Bahía Blanca, Argentina*
[c] *Centre for Research in Nanoengineering, Universitat Politècnica de Catalunya, Pasqual i Vila 15, 08028 Barcelona, Spain*

ARTICLE INFO

Article history:
Received 25 September 2012
Received in revised form
4 January 2013
Accepted 23 January 2013
Available online 28 February 2013

Keywords:
Hydrogen
Ethanol reforming
Monolith
Structured catalyst
Wall reactor

ABSTRACT

The present paper reports on the preparation, characterization and reaction evaluation of structured catalysts toward hydrogen generation via ethanol steam reforming. To these ends, 400 cpsi cordierite monoliths were functionalized with Rh–Pd/CeO_2 catalyst. SEM, TEM and XRD showed a uniform and well-covering CeO_2 layer where Rh–Pd nanoparticles of less than 0.5 nm were anchored. The functionalized monoliths were successfully tested for synthesis gas production from ethanol steam reforming. Realistic operating conditions were selected, including temperatures between 500 and 950 K, pressures from 1 to 6 bar, undiluted ethanol:water molar ratios 1:4–1:8 (i.e., $2 \leq S/C \leq 4$) and a wide range of feed loads. Appropriate activity and hydrogen selectivity were verified for the catalytic system, with ca. complete ethanol conversion at $T > 700$ K and a minor, or even negligible, generation of by-products (acetaldehyde, acetone, ethane, ethylene). Operating at 950 K and 1.5 bar, a H_2 yield of 3.4 mol hydrogen per mol ethanol in feed was achieved for a liquid feed load of 0.22 $\mu l_{liq}/(mg_{cat}$ min) ($S/C = 3$), with 8.1% of CH_4 and 8.2% of CO on dry basis. Kinetic parameters of a phenomenological set of reaction rate equations were fitted against experimental data, considering ethanol decomposition (methane formation) with subsequent methane steam reforming to both CO and CO_2 and water–gas shift reaction.

1. Introduction

The increasing demand of hydrogen as an energy vector moved researchers in the last two decades into the study of efficient ways to produce hydrogen from different feedstocks, to purify it up to the required degrees and to store it in proper conditions. Regarding the production methods, also the increasing concerns related to the potentials of employing environmentally friendly technologies pointed the use of ethanol (bioethanol) as raw material as it can be easily obtained from renewable sources. Moreover, its use leads to an almost-closed carbon dioxide cycle, strongly diminishing the net emissions to the atmosphere. Ethanol is additionally easy to handle and storage and presents low toxicity [1,2].

The steam reforming of ethanol (ESR) arises as a very attractive solution for supplying hydrogen when fuel cell

* *Corresponding author*. Institut de Tècniques Energètiques, Universitat Politècnica de Catalunya, Diagonal 647, ed. ETSEIB, 08028 Barcelona, Spain. Tel.: +34 934011708; fax: +34 934017149.
E-mail addresses: eduardo.lopez1@upc.edu (E. López), jordi.llorca@upc.edu (J. Llorca).
[1] Tel.: +34 934011708; fax: +34 934017149.
0360-3199/$ – see front matter
http://dx.doi.org/10.1016/j.ijhydene.2013.01.174

feeding is intended (e.g., of PEM type), while avoiding safety and storage issues related to other gaseous (hydrogen, methane) and liquid fuels (hydrogen, methanol). The direct feed to the reformer of diluted ethanol in water prevents the costs associated to extensive ethanol concentration [2]. Moreover, the ESR supposes maximizing the hydrogen yield as hydrogen is not only obtained from those in the ethanol but also the hydrogen in water is captured [3]. Numerous catalysts have been reported toward ESR, most of them based on nickel, cobalt and noble metals.

Ni-based catalysts are frequently used due to its C–C rupture capability and low cost. In contrast to noble metal, ESR over nickel-based catalysts takes place at moderate temperatures and their selectivity toward hydrogen increases as the temperature, the water:ethanol ratio and/or the nickel loading increase [4,5]. One cause of nickel-based catalysts deactivation is sintering of nickel particles under ESR reaction conditions and carbon deposition. Cobalt-based catalysts are less active for ESR than catalysts containing noble metals, but they are cheaper and very selective to H_2 and CO_2 since the reforming temperature can be as low as 623 K [6]. The reaction pathway is different from the one over noble metal and nickel catalysts since methane is not an intermediate of the reforming process allowing achieving high hydrogen yields at lower temperatures. However, these catalysts may suffer from great carbon formation under realistic reaction conditions.

In order to solve C deposition, many studies have been performed using noble metal-based catalysts because they are known to successfully break the C–C bond leading to less carbonaceous deposits and thus to more stable catalysts, provided that high enough temperatures are selected for reaction ($T > 850$ K). Rh, Pt, Pd, Ru, Ir and Ag as active phase have been investigated, in this order of relevance, as well as bimetallic catalysts [7–9]. Rh-based catalysts are the most used since this metal is the most effective one with respect to ethanol conversion and hydrogen selectivity [8,10,11]. Noble metals have been supported over a wide variety of supports (Al_2O_3, CeO_2, ZrO_2, Ce–Zr solid solutions, SiO_2, Y_2O_3, Nb_2O_5, MgO, TiO_2, C) and it has been found that the metal-support interaction prevents metal sintering and reduces coke formation. CeO_2-based supports are preferred due to ceria redox and oxygen storage properties. Over these supports, the reaction mainly proceeds in three consecutive steps with the increase of temperature, namely, ethanol decomposition, water–gas shift (WGS) reaction and methane steam reforming (MSR) [8].

The use of structured catalysts supposes appealing advantages over the use of powder or even pellets as channeling and/or blocking are highly prevented. The modular character of structured catalysts also suggests a straightforward scale-up of the reaction unit. Monolithic supports take advantages from these facts while the operation occurs with highly diminished pressure drops (2 or 3 orders of magnitude lower than those corresponding to pellets) [12].

This work presents a comprehensive experimental and theoretical study of the ESR over cordierite monoliths functionalized in our lab with an Rh–Pd/CeO_2 catalyst. We report first about the preparation and characterization of the structured catalysts, followed by details regarding their reaction evaluation facing changes in the operational variables, i.e., temperature, pressure, flowrate and inlet composition. Results of the stability tests are presented as well. Finally, aiming subsequent mathematical modeling, we report here the parameters of simple mass-action kinetics fitted to adjust our own laboratory measurements under a well-defined range of operating conditions of practical interest.

2. Experimental

2.1. Catalyst preparation

Conventional 400 cpsi (cells per square inch) cordierite monoliths (Corning Inc.) as cylinders of 1.8 cm diameter and length were used as support toward catalytic walls devices after functionalization with cerium oxide and rhodium–palladium as active metal. Following studies reported by Idriss et al. [8], 0.5%Rh–0.5%Pd over CeO_2 powder works properly for ethanol steam reforming, showing high activities and convenient selectivities provided that a high-enough operation temperature is selected. Each monolithic sample was first coated with ca. 250 mg of cerium oxide by repetitive immersion in an aqueous solution of $Ce(NO_3)_2 \cdot 6H_2O$ (Fluka), followed by 2 h drying at 353 K under continuous rotation (60 rpm) and calcination at 773 K for 5 h. Noble metals were then added in a single step by incipient wetness impregnation, using a water/acetone $PdCl_2$ and $RhCl_3$ solution (Sigma–Aldrich). Samples were dried at 373 K and calcined in air at 673 K for 4 h. More details regarding the catalyst preparation and characterization can be found elsewhere [8]. Before reaction, samples were reduced at 550 K for 1 h in 10% H_2/N_2.

2.2. Catalyst characterization

High resolution transmission electron microscopy (HRTEM) was performed with a JEOL 2010F microscope equipped with a field emission gun. The point-to-point resolution of the instrument was 0.19 nm and the resolution between lines was 0.14 nm. Samples were deposited from alcohol suspensions over grids with holey-carbon film. Scanning electron microscopy (SEM) was carried out at 5 kV using a Neon40 Crossbeam Station (Zeiss) equipped with a field emission (FE) SEM and a focused ion beam (FIB). FIB-cut (Ga+, 30 keV) grooves were made on the catalytic walls after previous e-beam and ion-beam assisted Pt deposition in order to estimate the thickness of the deposited Rh–Pd/CeO_2 layer. X-ray diffraction (XRD) measurements were performed with a Siemens D5000X diffractometer with Cu Kα incident radiation. XRD profiles were recorded from 3 to 75° (2θ) at a step size time of 18 s.

2.3. Catalytic tests

The reaction performance evaluation of the prepared monoliths was accomplished in a lab-scale kinetic set up, as shown in Fig. 1. The catalytic samples were implemented into a tubular stainless-steel reactor disposed in an electric furnace (Carbolite) governed with a PID electronic controller (Fuji PXR4). To avoid by-passes, high-temperature cement was used to fit the monolith to the reactor. The liquid feed mixture

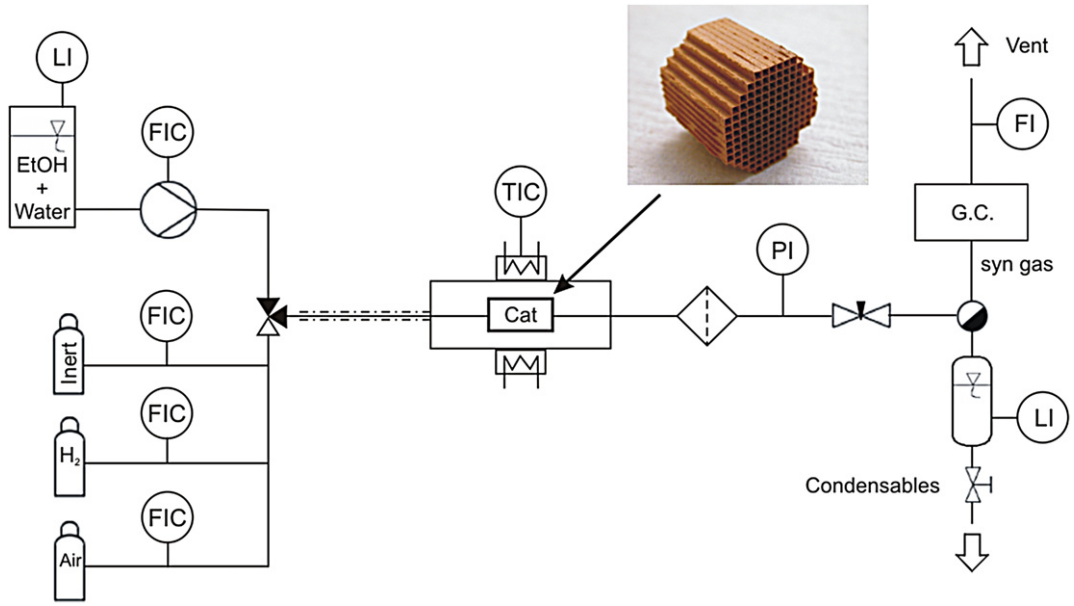

Fig. 1 – Schematic representation of the experimental set-up.

of ethanol and water was provided directly from a storage tank by an HPLC pump (Knauer Smartline). Alternatively, the feed to the reactor could be switched to a reducing/inert/oxidant gaseous stream. Heating tapes were used for feed evaporation and overheating sections before the furnace. A back-pressure regulator (Swagelok) was implemented after the reactor exit to set the desired operation pressure. After collecting the condensable components from the reactor, the gaseous effluent stream was quantitatively evaluated in terms of volumetric total flowrate (bubble soap meter) and composition. A micro GC (Agilent 3000A) equipped with MS 5Å, Plot U and Stabilwax capillary columns and TCD detectors was profited here to measure on-line gas concentrations every 5 min. Steady-state measurements of the catalyst performance were achieved under isothermal and isobaric conditions in the experimental set up described above. Realistic operating conditions were selected in this paper, with temperatures, reactants inlet concentrations, pressures and feed flowrates as reported in Table 1. Undiluted feeds (ethanol + water, no inerts) were used in all cases. Measurements were replicated 2–6 times with adequate reproducibility. H_2, CO_2, CO and CH_4 were the main reaction products. Minor fractions of acetaldehyde were detected for operation at low temperatures whereas negligible amounts of ethane, ethylene and acetone were measured by GC. Outlet molar flowrates of the non-condensable components (H_2, CH_4, CO_2, CO) were calculated from the measured composition (by GC) and total volumetric flowrate of the gaseous outlet stream, whereas outlet flowrates of ethanol and water (and acetaldehyde, if present) were evaluated by closing element balances. Operating at elevated temperature, where not even traces of ethanol and acetaldehyde were observed by GC, a carbon balance closure of maximum ±5% was verified, indicating additionally the absence of coke deposition. A total of 60 different experiences were performed. Additionally, uninterrupted long-term runs of >100 h were conducted to test for proper catalyst stability.

Table 1 – Experimental conditions.

Temperature [K]	500–950
Pressure [bar]	1.5–6
Feed load [μl_{liq}/(mg_{cat} min)]	0.21–1.08
Feed concentration [mol_{EtOH} : mol_{H_2O}]	1:4–1:8 (S/C = 2–4)

2.4. *Theoretical framework*

The reaction scheme shown below (Equations (1)–(4)) is proposed here to represent the results measured in the reaction experiences. According to the literature, over Rh–Pd/CeO_2 catalysts ethanol first decomposes into hydrogen, methane and carbon monoxide (Equation (1)) followed by the water–gas shift reaction (WGS, Equation (2)) [8,13]. The methane produced in reaction Equation (1) is further reformed (MSR) in presence of water at higher temperatures to CO or CO_2 as shown by reversible Equations (3) and (4) [14].

$$C_2H_5OH \rightarrow CO + CH_4 + H_2 \ (\Delta H_{298\ K} = 49.0\ kJ\ mol^{-1}) \quad (1)$$

$$CO + H_2O \leftrightarrow CO_2 + H_2 \ (\Delta H_{298\ K} = -41.2\ kJ\ mol^{-1}) \quad (2)$$

$$CH_4 + H_2O \leftrightarrow CO + 3H_2 \ (\Delta H_{298\ K} = 206.3\ kJ\ mol^{-1}) \quad (3)$$

$$CH_4 + 2H_2O \leftrightarrow CO_2 + 4H_2 \ (\Delta H_{298\ K} = 165.1\ kJ\ mol^{-1}) \quad (4)$$

Aiming subsequent reactor modeling, a simple global kinetic model is proposed to represent the synthesis-gas generation by ethanol steam reforming in the selected range of practical operating conditions. To this end, mass action type

rate equations have been assumed and the corresponding parameters were adjusted to fit the experimental data collected in the monolith evaluation. The fitting procedure was based upon a steady-state, 1-D, isothermal, pseudo-homogeneous mathematical model of the monolithic catalyst:

$$\frac{dF_j}{dz} = \rho_B \cdot A_T \cdot \sum_{i=1}^{4} \left(\gamma_{ji} \cdot r_i\right). \quad (5)$$

With $j = H_2$, CO_2, CO, CH_4 and i referring to Reactions (1)–(4). ρ_B has been defined as the catalyst loading per unit monolith volume; typical values of 5.5×10^4 g_{cat} m_R^{-3} were obtained. The differential equations representing the mass balances (Equation (5)) were solved by means of a Gear algorithm. The simple mass-action kinetics below proved to be sufficient to simulate the reactor behavior in the experimentally determined range of appropriate operating conditions:

$$r_1 = k_1 p_E \quad (6)$$

$$r_2 = k_2 \left[p_{CO} p_{H_2O} - \frac{p_{CO_2} p_{H_2}}{K_2}\right] \quad (7)$$

$$r_3 = k_3 \left[p_{CH_4} p_{H_2O} - \frac{p_{CO} p_{H_2}{}^3}{K_3}\right] \quad (8)$$

$$r_4 = k_4 \left[p_{CH_4} p_{H_2O}^2 - \frac{p_{CO_2} p_{H_2}{}^4}{K_4}\right] \quad (9)$$

$$k_i = k_{\infty,i} e^{-E_i/RT} \quad (10)$$

Equilibrium constants (K_i) in Equations (7)–(9) were adopted from Elnashaie and Elshishini [15]. The estimation of the kinetic parameters was performed using a nonlinear multiparametric regression algorithm [16]. The objective function minimized by the regression routine is shown in Equation (11). Pre-exponential factors and activation energies of Equations (6)–(10) were adjusted against 172 measured data (molar flowrates corresponding to 43 different experiences). Temperatures up to 825 K were used; experiences at higher temperatures were not considered for the fitting procedure to minimize the influence of diffusion effects.

$$\varphi = \sum_{e=1}^{N_{EXP}} \sum_{j=1}^{N_{COMP}} \left(F_{ej,calc} - F_{ej,exp}\right)^2 \quad (11)$$

where $N_{COMP} = 4$ and $N_{EXP} = 43$.

3. Results and discussion

3.1. Catalyst characterization

A detailed study of the microstructure of the catalyst was performed by high resolution transmission electron microscopy (HRTEM). In accordance to XRD results, lattice-fringe images of the CeO_2 support revealed the presence of (111), (200), (220) and (311) crystallographic planes of the fcc structure at 3.12, 2.71, 1.91 and 1.63 Å, respectively. In contrast, it was very difficult to identify Rh and/or Pd nanoparticles on the CeO_2 support. Fig. 2 shows representative HRTEM images of the catalyst, where highly dispersed particles with dimensions under 0.5 nm (marked by arrows) can be tentatively ascribed to metals entities given their high electron contrast with respect to CeO_2. Also, in profile view these entities are poorly defined and constituted by few atoms. Interestingly, they are concentrated on high Miller index planes ({311} in the image), whereas the more stable {111} planes are essentially metal-free. This is consistent with the higher energy of {311} crystallographic planes of CeO_2 compared to {111}, which are much less reactive [17].

Scanning electron microscopy (SEM) images were obtained directly on cordierite monoliths with the catalyst deposited as discussed above. After 2 h under reaction at 950 K and 0.81 μl_{liq}/(mg_{cat} min), a monolith was longitudinally cut and SEM images were acquired. Three adjacent channels with homogeneous catalyst coating are shown in Fig. 3a. Cordierite pores are visible, thus indicating that a thin ceria layer was deposited. A portion of the enclosed area in Fig. 3a is depicted in Fig. 3b and corresponds to a higher magnification image, where well-dispersed and uniform CeO_2 crystallites of ~30 nm (±7 nm) can be seen. The CeO_2 crystallites cover the whole cordierite surface and form a homogenous layer. Fig. 3c shows a groove made with an FIB-cut on the surface of a channel. The inner part (black zone) is the cordierite monolith substrate, which is

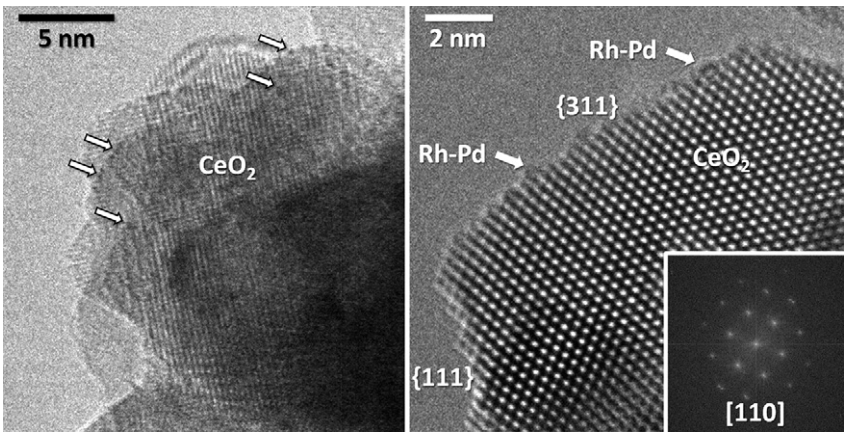

Fig. 2 – HRTEM images of the Rh–Pd/CeO_2 catalyst prepared in this work.

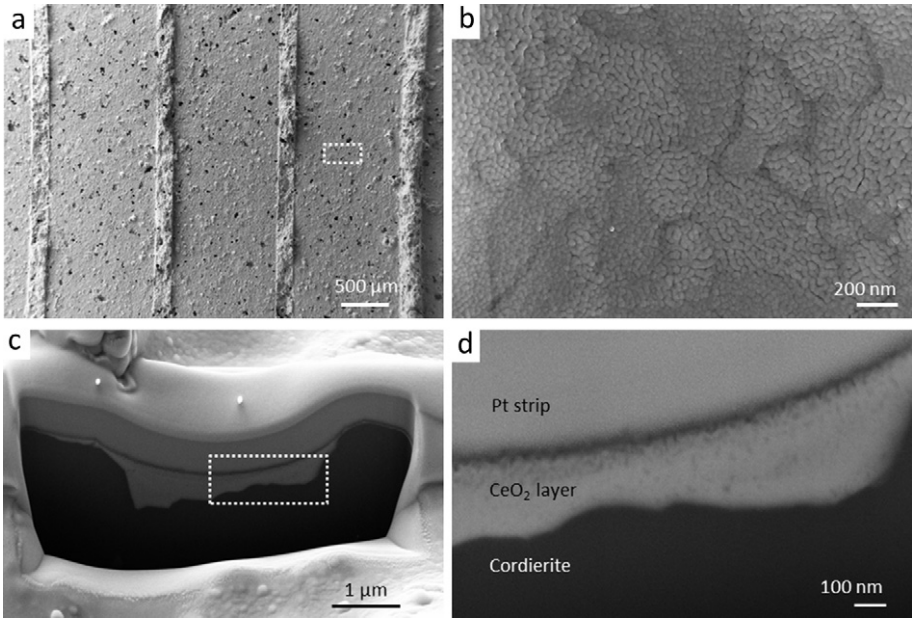

Fig. 3 – SEM images of the cordierite monolith functionalized with the Rh–Pd/CeO_2 catalyst.

covered with a CeO_2 layer that fills one of its pores. On top of the CeO_2 layer, Pt strips can be differentiated which correspond to Pt deposition to perform a clean FIB-cut. Fig. 3d displays a higher magnification image of the area enclosed in Fig. 3c and corresponds to a detailed view of the layers' profile made with the FIB-cut. The CeO_2 layer is homogeneous, uniform, and well-adhered and fills perfectly the cordierite pore. The thickness varies between 100 and 200 nm and it is possible to observe the texture of this layer. No carbon deposits were observed and no differences with the fresh monolith (SEM images not shown here) were noticed.

3.2. *Ethanol steam reforming*

Molar flowrates of different species from the reactor operating at different temperatures are reported in Fig. 4. At temperatures in the order of 600 K, the product distribution shows almost similar amounts of H_2, CO and CH_4, indicating that ethanol decomposition is the only reaction reaching a significant extent. Experimental points at 700 K show additionally the occurrence of the water gas shift reaction (Equation (2)), resulting in CO_2 appearance in detriment of CO. Accordingly, an important increase in H_2 is observed. Further temperature increases promote methane steam reforming yielding higher amounts of hydrogen and methane consumption. At the higher temperatures essayed, a non desired CO increase is measured due to the equilibrium nature of the exothermic water gas shift reaction. No other by-products (e.g. acetaldehyde) were detected here.

Fig. 5 shows the ethanol conversion (x_{EtOH}) achieved in the monolithic catalyst for different operation temperatures and pressures. The corresponding hydrogen yields (η), as calculated following Equation (12), are reported as well.

$$\eta = \frac{F_{H_2}}{F_{EtOH,f}} \tag{12}$$

As observed, x_{EtOH} increases with T, reaching 100% ethanol conversion for temperatures higher than 700 K for the selected operating conditions. The increase of x_{EtOH} with pressure for temperatures lower than 700 K (e.g., for $T = 600$ K, Fig. 5) is consistent with a positive reaction order for ethanol decomposition, as reported in Equation (6). The same effect is observed for hydrogen yields. Conversely, when operation at higher temperatures is selected, higher pressures render lower η, as the methane steam reforming (Equations (3) and (4)) reactions are prevented due to increasing equilibrium limitations.

Fig. 6 presents methane molar flowrates evolved from the monolithic reactor for the same conditions as in Fig. 5. As seen, methane represents both a reaction product (Equation (1)) and a reactant–product (reversible Equations (3) and (4)). At low temperatures the reaction rates of methane steam reforming reactions are negligible compared to ethanol decomposition and methane is observed as a reaction product,

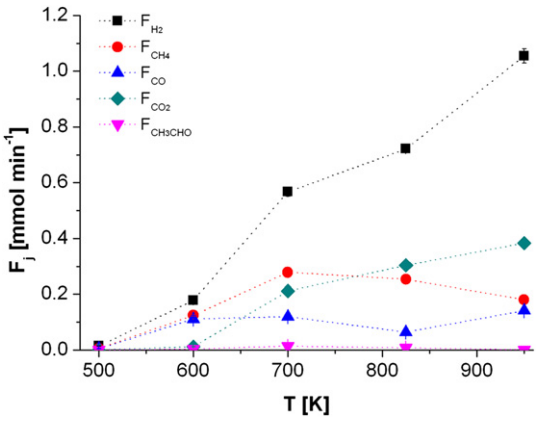

Fig. 4 – Influence of reaction temperature on the molar flowrates of the main reaction products. S/C = 3, P = 3.0 bar, Load = 0.22 $\mu l_{liq}/(mg_{cat}$ min).

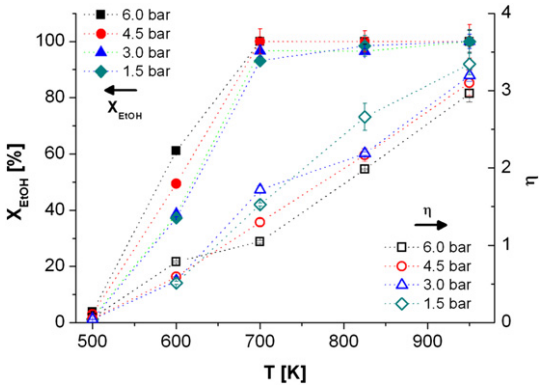

Fig. 5 – Influence of reaction temperature on ethanol conversions (solid symbols) and hydrogen yields (empty symbols) for different operation pressures. S/C = 3, Load = 0.22 $\mu l_{liq}/(mg_{cat}$ min).

with increasing methane formation for higher pressures, as expected. At intermediate temperatures (e.g., $T = 700$ K), methanation occurs to some extent, favored by higher pressures. Again, higher temperatures promote methane steam reforming and all the ethanol fed is converted to methane and further reacted to CO/CO_2. The same implications for the effect of pressure discussed above for η apply here for F_{CH_4}.

Fig. 7 reports, for the different operating temperatures selected, the influence of the feed composition (S/C) over the exit flowrates of H_2 (a), CO (c) and CO_2 (d) and the hydrogen yields (b). At low temperatures, where the methane reforming is not favored, higher equilibrium displacements in the water gas shift reaction for higher water contents compensate lower amounts of ethanol fed (at constant liquid feed load), as seen in the zoom shown in Fig. 7a. Additionally, methanation is also prevented at higher water contents due to equilibrium limitations, rendering more hydrogen. When temperatures are high enough to promote MSR, the dilution effect clearly prevails and increased flowrates for all three H_2, CO and CO_2 are attained for higher ethanol loads (less diluted feeds). On the other hand, hydrogen yields (see Fig. 7b) reveal a superior reaction performance for higher S/C for the whole temperature range under study. For the highest temperature selected, S/C higher than 3 revealed of minor influence in terms of H_2 yield and appears not convenient to limit the economic cost related to the evaporation and overheating of the excess water.

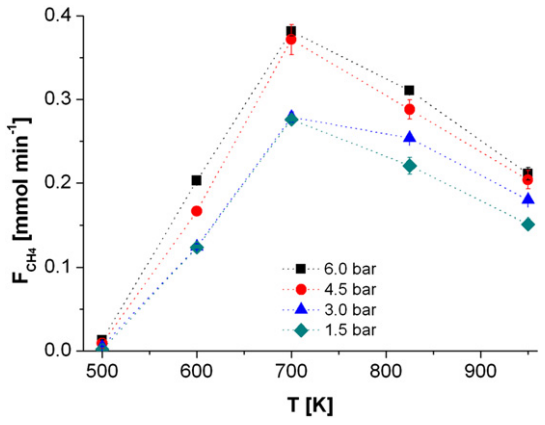

Fig. 6 – Influence of reaction temperature on methane flowrates at the reactor exit for different operation pressures. S/C = 3, Load = 0.22 $\mu l_{liq}/(mg_{cat}$ min).

A study of the effect of the liquid load on the catalytic performance of the functionalized monoliths was performed as well. Fig. 8a presents ethanol conversions, hydrogen yields and hydrogen molar flowrates for increasing liquid feed load (per unit mass catalyst). Complementary, Fig. 8b shows selectivities on a dry basis to the main reaction products (H_2, CO, CO_2 and CH_4; the selectivity toward acetaldehyde was kept under 0.7% in all cases). As observed in Fig. 8a, ethanol conversion maintains certain constancy for the first loads selected while a light drop in conversion is calculated as higher loads are assayed due to the reduced residence times at hand. Hydrogen yields show a more pronounced drop as they result not only from the ethanol conversion but also from the methane reforming and WGS reactions. Higher loads lead to higher total amounts of hydrogen produced as long as the reactions maintain their extents (see lower loads). For the higher loads selected the H_2 molar flowrates balance as a product of higher amounts of ethanol available and diminished extents of the reactions involved (Equations (1)–(4)). Fig. 8b shows the remarkable influence of the residence time on the extent of the water–gas shift reaction (Equation (2)), from very appropriate values of CO selectivity of ca. 3% for reduced loads to higher amounts of CO than those of CO_2 for the higher inlet flowrates selected. In this last scenario, a shift reactor of considerable dimensions (or two high and low temperature shift reactors) should be installed after the reformer to meet the recommended maximum inlet CO concentrations of ca. 2% for usual $CO–PrO_x$ reactors [18]. Conversely to CO and CO_2 behaviors, methane selectivity remains almost invariant for the selected range of incoming feed flowrates. Values in the order of 20% selectivity points here a loss of hydrogen, as also reflected on the yields up to 2 mol_{H_2}/mol_{EtOH} reported in Fig. 8a; operation at higher temperatures would be desirable in this situation to promote higher rates of methane reforming.

Experiences regarding the shut down and start up of the reaction under inert atmosphere were also conducted. In fact, under normal operation at steady-state, the feed was suddenly changed by inert gas and the furnace was cooled down to room temperature under this atmosphere. After resting in this situation for 20 h, the electric furnace was led again up to reaction temperature while maintaining the inert feed. When the desired temperature (e.g., $T = 825$ K) was reached, the feed was switched back to the usual ethanol/water liquid mixture ($S/C = 3$) and the operation performance measured prior to the introduction of inert gas was immediately recovered.

Long-term experiences of uninterrupted >100 h on stream were also performed to investigate the catalyst stability. Intermediate operation temperature of $T = 773$ K was selected with $P = 4.5$ bar and liquid mixture $S/C = 3$. A high load of 0.47 $\mu l_{liq}/(mg_{cat}$ min) was used here. Fig. 9 presents the results of this stability test, indicating constancy on the catalytic performance up to ca. 75 h operation. In fact, while achieving complete ethanol conversion and after a slight activation period, mean values of 2.1 mol_{H_2}/mol_{EtOH} for the hydrogen yield, with approximately 16% CH_4, 3% CO and 0.3%

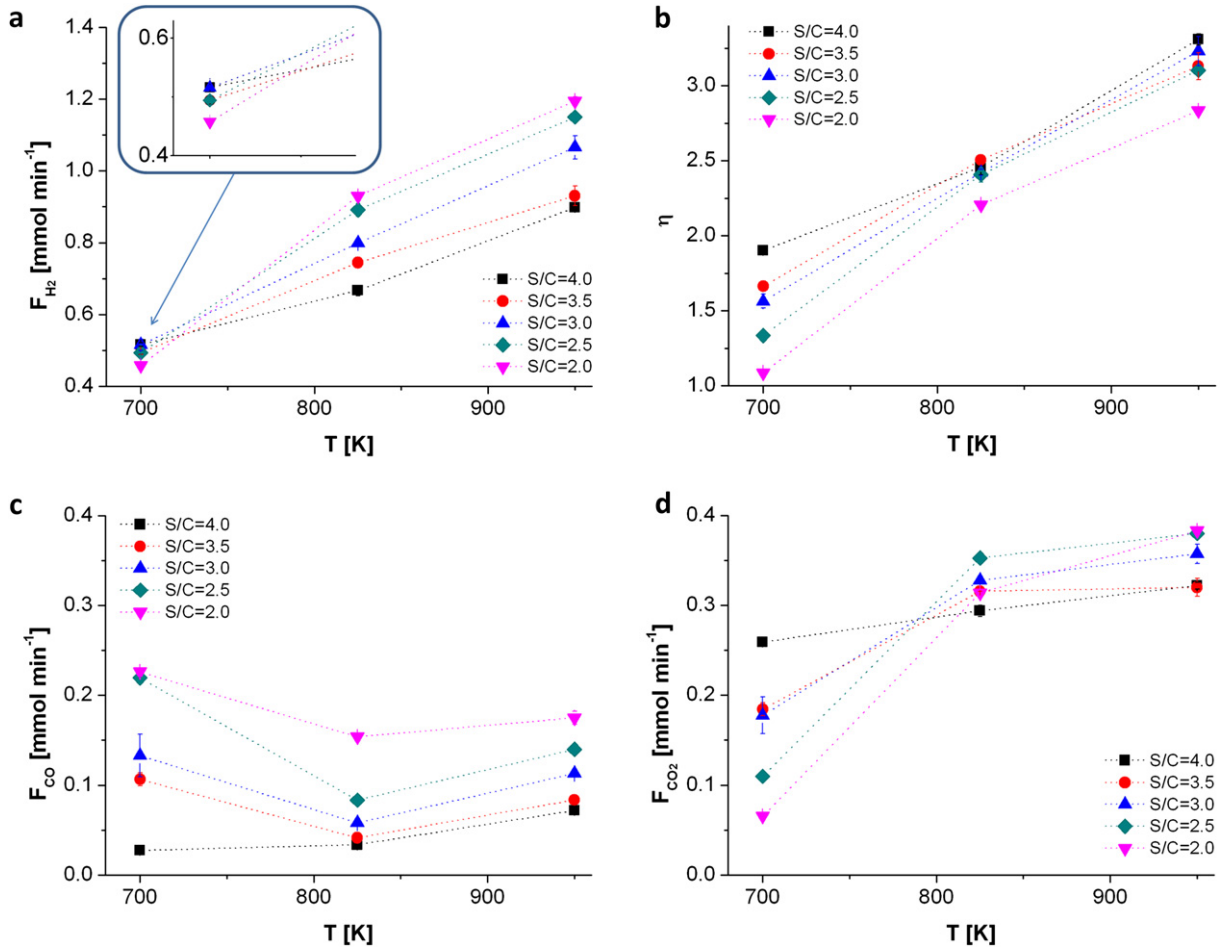

Fig. 7 – Influence of reaction temperature for different feed compositions (as S/C) on the exit molar flowrates of hydrogen (a), carbon monoxide (c), and carbon dioxide (d), as well as on the hydrogen yield (b). P = 4.5 bar, Load = 0.22 μl_{liq}/(mg_{cat} min).

acetaldehyde selectivities were measured. From 75 h onwards on stream the total volumetric flowrate of the gaseous outlet stream as well as the selectivity to the main gaseous products both deteriorate rapidly, leading to a drop in ethanol conversion. These observations were accompanied by a noticeable increase of byproducts at the reactor outlet, namely, acetaldehyde, acetone and C_2 species. At around 120/130 h of continuous operation the catalyst activity was almost

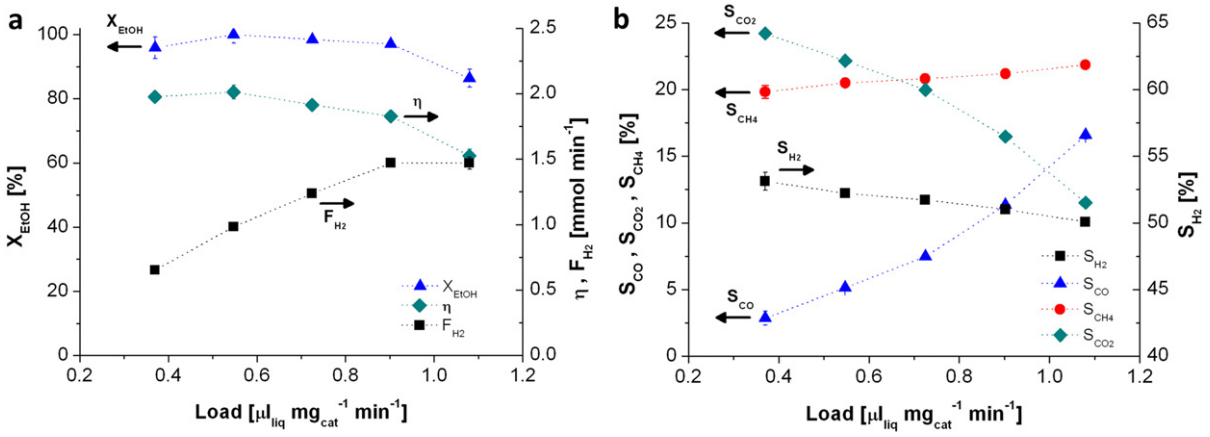

Fig. 8 – a. Influence of the feed load on ethanol conversion (▲), hydrogen molar flowrate (■) and hydrogen yield (◆). S/C = 3, P = 4.5 bar, T = 773 K. b. Influence of the feed load on the selectivity to the main reaction products. S/C = 3, P = 4.5 bar, T = 773 K.

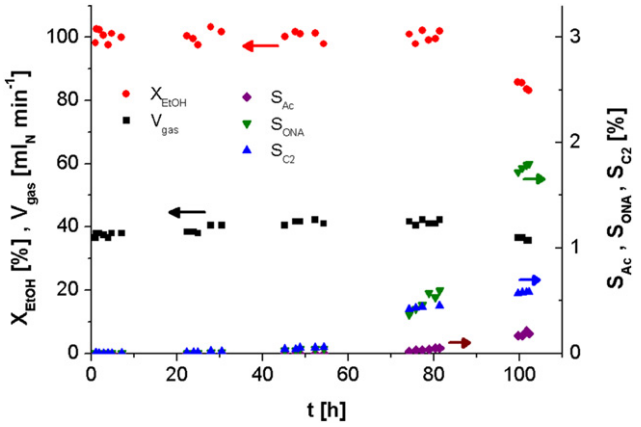

Fig. 9 – Ethanol conversion, outlet volumetric gas flowrate and selectivity to byproducts for >100-h stability test. S/C = 3, P = 4.5 bar, T = 773 K, Load = 0.47 $\mu l_{liq}/(mg_{cat}$ min).

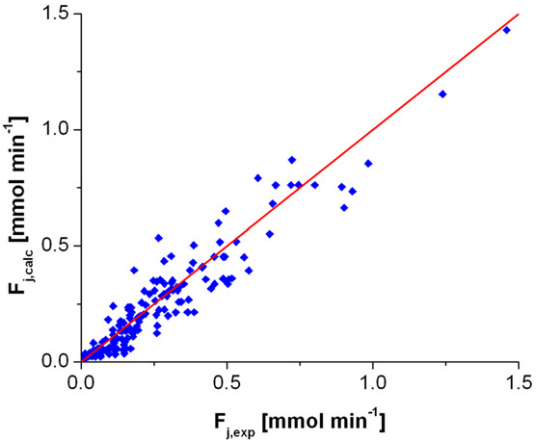

Fig. 10 – Parity plot for calculated vs. experimental exit molar flowrates using the estimated parameters reported in Table 2 (the solid line represents the identity).

Table 2 – Estimated parameters for reaction rates 1–4.

Reaction i	$k_{\infty,i}$ [mol/(mg_{cat} min bar^n)]	E_i [kJ mol^{-1}]
1	4.3×10^{1}	87
2	3.6×10^{-1}	70
3	5.3×10^{2}	154
4	5.2×10^{3}	156

completely lost (results not shown here). Preliminary results showed that this deactivation phenomenon could be reverted by 30 min operation under a feed containing 5% O_2 diluted in inert at 773 K; a peak of CO_2 was measured by GC at the reactor outlet during the oxidation. Usual catalytic performance was completely recovered after this treatment indicating the probable occurrence of combustion of a surface deposit (coke) blocking the catalyst active sites.

3.3. *Reaction model*

As already discussed in Section 2.4, aiming to represent the measured experimental data and for subsequent mathematical modeling, activation energies and pre-exponential factors of simple mass-action kinetics (see Equations (6)–(10)) were fitted. Table 2 reports the adjusted parameters within this contribution. In Table 3 we report data toward a comparison of the fitted activation energies as well as other catalyst details with references among the literature regarding ESR over noble metal-based catalysts with reported kinetic parameters. As easily seen, only less than half of the listed works report kinetic parameters able to quantitatively describe the products distribution; i.e., a set of reactions with stated kinetics. The remaining works only follows the ethanol consumption, which proves not enough when a reactor has to be dimensioned to fulfill the hydrogen requirements of, e.g., a fuel cell or to accomplish the design of the purification units downstream the reformer (water–gas shift reactor/CO–PrO_x reactor). As also noticed from Table 3, the catalysts reported in the majority of the publications there lack of a support allowing a modular character and diminished pressure drop. Regarding the catalyst formulation, it has been demonstrated elsewhere [8] that a bimetallic Rh–Pd or Rh–Pt catalyst deserved superior performance for ESR when compared with a monometallic Rh or Pd (or Pt) based catalyst due to the valuable combination of the improved capacities of Rh to dissociate the C–C bond and

Table 3 – Compilation of literature studies regarding ESR over catalysts based on noble metals with reported kinetic parameters.

Reference	Catalyst	Origin	Support	Kinetics for Rx #/E_i [kJ mol^{-1}]
This work	Rh–Pd/CeO_2	Prepared	Monolith	1, 2, 3, 4/87, 70, 154, 156
[13]	Rh–$MgAl_2O_4/Al_2O_3$	Prepared	Pellets	1, 13[a], 2, 3/85.9, 418, 151, 107
[19]	Pd-based	Commercial	Metal sheet	13[a], 2, 3/148, 59.9, 107.3
[20]	Pt/CeO_2	Prepared	Powder	[b]/18.4
[21]	Pt–Ni/Al_2O_3	Prepared	Powder	[b]/59.3
[22]	Pt–Ni/Al_2O_3	Prepared	Powder	[b]/39.3
[23]	Ru/Al_2O_3	Commercial	Pellets	[b]/96
[24]	Rh–Pt/Zr-based	Commercial	Monolith	[b]/85
[25]	Rh/CeO_2	Prepared	Microreactor	1, 2, 3/558, 496, 400

a Rx #13: $C_2H_5OH + H_2O \rightarrow CO_2 + CH_4 + 2H_2$.
b Only ethanol reaction rate evaluated (ethanol consumption).

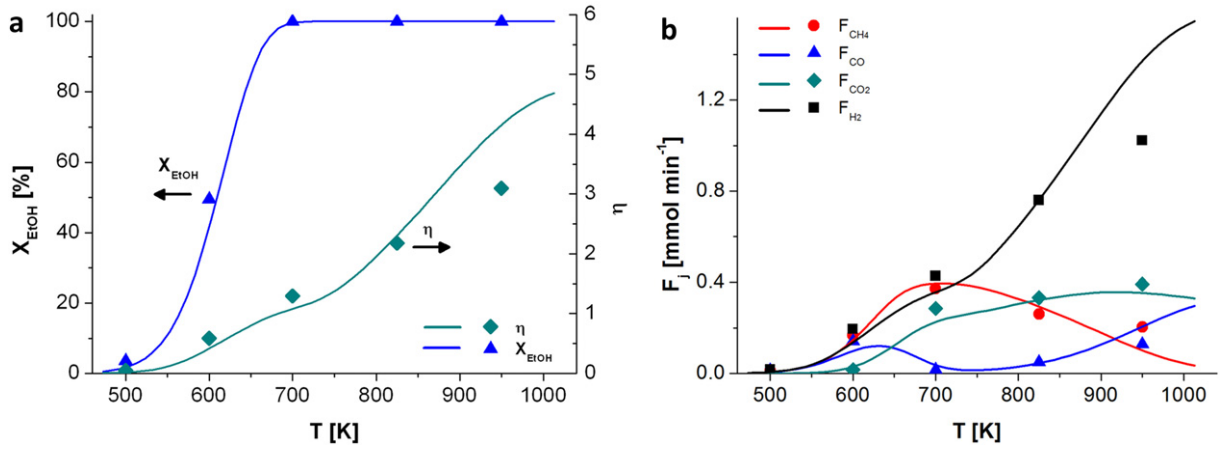

Fig. 11 – a. Experimental (points) and calculated (lines) ethanol conversions and hydrogen yields. $P = 4.5$ bar, $S/C = 3$, Load $= 0.22$ $\mu l_{liq}/(mg_{cat}$ min). b. Experimental (points) and calculated (lines) exit molar flowrates for the main reaction products. $P = 4.5$ bar, $S/C = 3$, Load $= 0.22$ $\mu l_{liq}/(mg_{cat}$ min).

of Pd (or Pt) for the H–H recombination. Moreover, the deposition of the sub-nanometric Rh and Pd particles over well-dispersed and uniform CeO_2 crystallites of ~30 nm in size accomplished here points to a superior catalyst formulation if compared to more traditional preparations using alumina as support due to an enhanced capacity of reducing the coke formation (via suppression of the ethylene production).

A comparison of the obtained activation energies with the ones shown in Table 3 is not completely straightforward. As mentioned, not all the publications there propose a set of reactions and provide the correspondent kinetic parameters. Instead, some of them only describe the ethanol consumption. Focusing on the activation energy for ethanol decomposition (Rx#1), a value fitted here of 87 kJ mol^{-1} agrees well with the one of Ref. [13] and, if assumed that the ethanol disappearance quantified in Refs. [20–24] of Table 3 could be associated with ethanol decomposition, our E_1 agrees also with Ref. [24] and in a less degree with [23]. Refs. [20] and [22] seem to have some kind of mass transport phenomenon associated due to the low values reported. The value fitted here for the activation energy of the water–gas shift reaction is in the range of the correspondent of Ref. [19], both considerably lower than the reported in [13] and [25]. In fact, all E_i reported by Ref. [25] appears surprisingly high. A reported activation energy for MSR to CO (see Equation (3)) of 151 kJ mol^{-1} in Ref. [13] is close to the one here of 154 kJ mol^{-1}. The relation between activation energies of the MSR to CO and to CO_2 (Equations (3) and (4)) fitted in this work is in the order of the one reported by Xu and Froment (Ni-based catalyst [14]), being these last two higher (240 and 242 kJ mol^{-1}, respectively) given the lower activity of Ni when compared to noble metals.

Fig. 10 shows a parity plot comparing the measured and calculated molar flowrates of H_2, CO_2, CO and CH_4 for all the experiences considered in the fitting procedure. A global standard deviation of 0.503 was calculated. The influence of the operation temperature on both experimental and calculated ethanol conversions and hydrogen yields is presented in Fig. 11a to show the accuracy of the adjusted parameters in reproducing the measured data. Fig. 11b complementary reports molar flowrates of the main reaction products. As seen, a very reasonable match of the model predictions to the observed data was attained. Again, for low temperatures the sole effect of ethanol decomposition renders similar amounts of H_2, CH_4 and CO. At intermediate temperatures the effect of the WGS (Equation (2)) leads to higher amounts of CO_2 and extra hydrogen. Methanation is also observed since hydrogen does not increase as much as should point the CO_2 appearance and extra methane appear from considering only ethanol decomposition. At higher temperatures, methane reforming is promoted along with increasing CO due to the equilibrium shift of the water gas shift reaction (the reverse WGS produces more CO at expenses of CO_2 and H_2). Experimental molar flowrates and yields of hydrogen at the highest temperature (i.e., $T = 950$ K) are overestimated by the adjusted kinetics. As pointed in Section 2.4, these points were not included in the set of fitted data to minimize the influence of diffusion effects.

4. Conclusions

A 0.5%Rh–0.5%Pd over CeO_2 catalyst was deposited over 400 cpsi cordierite monoliths aiming hydrogen generation by ethanol steam reforming. The resultant structured catalysts were characterized by SEM, TEM and XRD, which revealed the existence of a well-adhered and homogenous CeO_2 coverage of the cordierite monolith with Rh–Pd nanoparticles smaller than 0.5 nm. The reaction evaluation of the functionalized monoliths was conducted in a kinetic set-up at realistic operating conditions. Appropriate activity and hydrogen selectivity were verified for the catalytic system, with ca. complete ethanol conversion at $T > 700$ K and no generation of by-products (acetaldehyde, ethane, ethylene). Operating at 950 K and 1.5 bar, a H_2 yield of 3.4 mol_{H_2}/mol_{EtOH} was achieved for a liquid feed load of 0.22 $\mu l_{liq}/(mg_{cat}$ min) ($S/C = 3$), with 8.1% of CH_4 and 8.2% of CO on a dry basis. Catalytic performance is kept constant for uninterrupted 75 h on stream. After this, a deactivation process is observed, which can be completely reverted by oxidation. Parameters from simple mass action kinetics were fitted against the experimental data

achieving a satisfactory match between measured and calculated molar flowrates. Prevented that no extrapolation is intended outside the range of operating conditions used in the fitting, the system of adjusted reaction rates appears able to catch the qualitative catalyst response facing changes in temperature, pressure and/or feed conditions (concentration and load). An appropriate quantitative description of the measured molar flowrates of the main reaction products is achieved as well. Summing up, both the remarkable importance of the addressed research topic along with such a broad study, from the catalyst preparation to the kinetics analysis, pose a remarkable novelty on the present contribution. The studies reported here point the use of monolithic catalysts coated with Rh–Pd/CeO_2 as technologically attractive for the generation of a hydrogen-rich stream from ethanol steam reforming. The combination of: a) a very interesting catalytic performance; b) the modular character, mechanical stability and operation advantages of the monoliths; and c) the development of theoretical tools as adjusted reaction rates to help in the reactor design, suggests a viable practical implementation of this system.

Acknowledgments

This work has been carried out with the support of MICINN, projects CTQ2009-12520 and PRI-AIBAR-2011-1092, MINCYT-MICINN project ES/11/07, and MINECO project ENE2012-36368. N.J.D. is grateful to UPC and Digema Technologies, S.L. for a PhD grant. J.L. acknowledges ICREA Academia program.

Nomenclature

A_T	cross sectional area of monolith, m^2
E	activation energy, kJ mol^{-1}
F	molar flowrate, mol min^{-1} or mmol min^{-1}
k	reaction rate constant, mol min^{-1} g_{cat}^{-1} bar^{-n}
k_∞	pre-exponential factor, mol min^{-1} g_{cat}^{-1} bar^{-n}
K	equilibrium constant
N_{COMP}	number of components in fitting
N_{ExP}	number of experiments in fitting
P	pressure, bar (absolute)
r	reaction rate, mol min^{-1} g_{cat}^{-1}
R	universal gas constant, kJ mol^{-1} K^{-1}
S	selectivity
S/C	steam-to-carbon ratio in feed
T	temperature, K
V_{gas}	total volumetric flowrate of the gaseous outlet stream, ml_N min^{-1}
x_{EtOH}	ethanol conversion
z	axial coordinate, m

Subindex

Ac	acetaldehyde
calc	calculated by math model
cat	catalyst
C_2	ethane + ethylene
CH_4	methane
CO	carbon monoxide
CO_2	carbon dioxide
e	experiment number
exp	experimental
H_2	hydrogen
f	feed
i	reaction *i*
j	component *j*
liq	liquid
ONA	acetone
R	reactor

Greek letters

ρ_B	catalyst density, g_{cat} m_R^{-3}
ϕ	objective function in fitting, see Equation (11)
η	hydrogen yield, see Equation (12)
γ_{ji}	stoichiometric coefficient of component *j* in reaction *i*

REFERENCES

[1] Frusteri F, Freni S. Bio-ethanol, a suitable fuel to produce hydrogen for a molten carbonate fuel cell. J Power Sources 2007;173:200–9.
[2] Vaidya P, Rodrigues A. Insight into steam reforming of ethanol to produce hydrogen for fuel cells. Chem Eng J 2006; 117:39–49.
[3] Ni M, Leung D, Leung M. A review on reforming bio-ethanol for hydrogen production. Int J Hydrogen Energy 2007;32: 3238–47.
[4] Li MS, Wang XD, Li SR, Wang SP, Ma XB. Hydrogen production from ethanol steam reforming over nickel based catalyst derived from Ni/Mg/Al hydrotalcite-like compounds. Int J Hydrogen Energy 2010;35(13):6699–708.
[5] Wang W. Production of hydrogen by steam reforming of bioethanol over copper–nickel bimetallic catalysts. Int J Green Energy 2009;6(1):92–103.
[6] Llorca J, Homs N, Sales J, Ramírez de la Piscina P. Efficient production of hydrogen over supported cobalt catalysts from ethanol steam reforming. J Catal 2002;209:306–17.
[7] Sanchez-Sanchez MC, Navarro Yerga R, Kondarides D, Verykios X, Fierro JL. Mechanistic aspects of the ethanol steam reforming on Pt, Ni and PtNi catalysts supported on γ-Al_2O_3. J Phys Chem A 2010;114:3873–82.
[8] Idriss H, Scott M, Llorca J, Chan S, Chiu W, Sheng P, et al. A phenomenological study of the metal-oxide interface: the role of catalysis in hydrogen production from renewable resources. ChemSusChem 2008;1:905–10.
[9] Scott M, Goeffrey M, Chiu W, Blackford MA, Idriss H. Hydrogen production from ethanol over Rh–Pd/CeO_2 catalysts. Top Catal 2008;51:13–21.
[10] Diagne C, Idriss H, Kiennemann A. Hydrogen production by ethanol reforming over Rh/CeO_2–ZrO_2 catalysts. Catal Commun 2002;3:565–71.
[11] Romero-Sarria F, Vargas JC, Roger A-C, Kiennemann A. Hydrogen production by steam reforming of ethanol. Catal Today 2008;133–135:149–53.
[12] Cybulski A, Moulijn J. Structured catalysts and reactors. New York: Marcel Deker Inc.; 1998.
[13] Graschinsky C, Laborde M, Amadeo N, Le Valant A, Bion N, Epron F, et al. Ethanol steam reforming over Rh(1%)$MgAl_2O_4$/Al_2O_3: a kinetic study. Ind Eng Chem Res 2010;49:12383–9.

[14] Xu J, Froment G. Methane steam reforming, methanation and water gas shift: I. Intrinsic kinetics. AIChE J 1989;35:88–103.
[15] Elnashaie S, Elshishini S. Modeling, simulation and optimization of industrial fixed bed catalytic reactors. London: Gordon and Breach Science; 1993.
[16] Marquardt D. An algorithm for least-squares estimation of nonlinear parameters. J Soc Ind Appl Math 1963;11(2):431–41.
[17] Aneggi E, Llorca J, Boaro M, Trovarelli A. Surface-structure sensitivity of CO oxidation over polycrystalline ceria powders. J Catal 2005;234:88–95.
[18] López E, Kolios G, Eigenberger G. Preferential oxidation of CO in a folded-plate reactor. Chem Eng Sci 2007;62:5598–601.
[19] Lopez E, Gepert V, Gritsch A, Nieken U, Eigenberger G. Ethanol steam reforming thermally coupled with fuel combustion in a parallel plate reactor. Ind Eng Chem Res 2012;51(11):4143–51.
[20] Ciambelli P, Palma V, Ruggiero A. Low temperature catalytic steam reforming of ethanol. 2. Preliminary kinetic investigation of Pt/CeO_2 catalysts. App Catal B: Environ 2010;96(1–2):190–7.
[21] Soyal-Baltacıoğlu F, Aksoylu AE, Önsan Z. İ. Steam reforming of ethanol over Pt–Ni catalysts. Catal Today 2008;138:183–6.
[22] Örücü E, Gökaliler F, Aksoylu AE, Önsan Z. İ. Ethanol steam reforming for hydrogen production over bimetallic Pt–Ni/Al_2O_3. Catal Lett 2008;120(1–2):198–203.
[23] Vaidya PD, Rodrigues AE. Kinetics of steam reforming of ethanol over a Ru/Al_2O_3 catalyst. Ind Eng Chem Res 2006;45(19):6614–8.
[24] Simson A, Waterman E, Farrauto R, Castaldi M. Kinetic and process study for ethanol reforming using a Rh/Pt washcoated monolith catalyst. App Catal B: Environ 2009;89(1–2):58–64.
[25] Görke O, Pfeifer P, Schubert K. Kinetic study of ethanol reforming in a microreactor. App Catal A: Gen 2009;360(2):232–41.